Journal of Computational Physics **174,** 492–509 (2001)
doi:10.1006/jcph.2001.6885, available online at http://www.idealibrary.com on IDEAL®

An Unstructured *hp* Finite-Element Scheme for Fluid Flow and Heat Transfer in Moving Domains

Ali Beskok*,[1] and Timothy C. Warburton†,[2]

*Mechanical Engineering Department, Texas A&M University, College Station, Texas 77843; and †Division of Applied Mathematics, Brown University, Providence, Rhode Island 02912

Received February 8, 2000; revised March 1, 2001

This paper presents the formulation, validation, and application of a spectral/*hp* algorithm for numerical solution of the Navier–Stokes and heat/scalar transport equations in arbitrarily moving complex geometries. The new spectral element algorithm is based on the arbitrary Lagrangian Eulerian formulation and utilizes modal expansion of Jacobi polynomials in mixed triangular and quadrilateral elements in two dimensions. Time integration is performed by stiffly stable schemes and can deliver up to third-order time accuracy for transient problems. Test cases with sufficiently smooth solutions demonstrate spectral convergence and low phase/dissipation error. Preliminary simulation results for micro-mixers and micro-heat spreaders are also presented.

Key Words: spectral element; *hp* methods; ALE formulation; micro-mixers; micro heat spreaders.

1. INTRODUCTION

Fluid flow and heat transfer in arbitrarily moving complex geometries are observed in various engineering applications. A predominant example is the micro electromechanical systems (MEMS), where the device components exhibit high-frequency oscillations with micron-scale clearances [1, 2]. Experimentation and validation in micro-scales are challenging and expensive. Therefore, robust numerical simulation tools can be used to predict the performance of a micro-system design prior to the fabrication of hardware. Numerical simulation tools for micro-system design should be able to analyze coupled fluid/structure interaction, heat/species transport problems in complex arbitrarily moving

[1] To whom correspondence should be addressed. E-mail: abeskok@mengr.tamu.edu.

[2] Present address: Department of Mathematics and Statistics, The University of New Mexico, Albuquerque, New Mexico 87131-1141.

0021-9991/01 $35.00

geometries, with reasonable time and space accuracy. These algorithms should also include micro-scale-specific models, such as velocity slip for gas and electrokinetic effects for liquid micro-flows [3–5].

An overall computational approach to MEMS and various other scientific and engineering problems requires multidisciplinary simulation capabilities, robust treatment of moving boundaries, geometric flexibility, and computational accuracy. Unstructured *hp* finite-element methods, delivering high-order accuracy and flexibility to discretize complex geometry, usually satisfy the last two requirements [6–8]. Robust treatment of the moving boundary requirement can be satisfied by the arbitrary Lagrangian Eulerian (ALE) formulation, where the arbitrary motion and acceleration of the moving domain can be handled independent of the fluid motion. The ALE method was developed in the early 1970s for fluid flow problems in arbitrarily moving domains [9]. Hughes *et al.* [10] and Donea *et al.* [11] developed finite-element-based ALE formulations for incompressible viscous flows to study dynamic fluid structure interaction problems (see also [12]). Further advances in the ALE method, especially in improvement of the mesh velocities for moving boundaries, have been developed by Lohner and Yang [13]. The first spectral element ALE algorithm was developed by Ho, using quadrilateral spectral elements to study free surface flows [14]. In the meantime, Sherwin and Karniadakis developed an unstructured spectral/*hp* finite-element algorithm $\mathcal{N}\varepsilon\kappa\mathcal{T}\alpha\boldsymbol{r}$, which utilized triangular and tetrahedral elements for two- and three-dimensional fluid flow problems [6, 7]. Warburton extended $\mathcal{N}\varepsilon\kappa\mathcal{T}\alpha\boldsymbol{r}$ to include mixed triangular and quadrilateral elements for two-dimensional and mixed tetrahedra, pyramid, prism, and hexahedra for three-dimensional fluid flow problems [15]. Using this approach, we developed an unstructured *hp* element ALE algorithm for solving the two-dimensional incompressible Navier–Stokes and heat transfer/scalar transport equations in moving domains. We present here the benchmark studies of time and space accuracy of our scheme, including a study of its combined phase and dissipation error characteristics for long time integration. We also present a series of micro-fluidic applications, which demonstrate robustness of the new algorithm under large mesh distortions. The principle demonstrated here is that the ALE approach using unstructured spectral elements is robust and has great potential in numerical simulation of flow and heat transfer in moving domains.

This paper is organized as follows: Section 2 presents the new ALE formulation for solution of the Navier–Stokes and scalar transport equations. Section 3 validates the new algorithm and demonstrates its space, time, and phase accuracy. Section 4 presents simulation results for a micro-mixer and the micro heat spreader (MHS). Section 5 summarizes and concludes our work.

2. ALE FORMULATION OF INCOMPRESSIBLE NAVIER–STOKES AND SCALAR TRANSPORT EQUATIONS

In this section, we consider domains that are arbitrarily moving in time. This is not a trivial generalization because we have to discretize the time-dependent operators as well as the time-dependent fields. In the ALE formulation, the local elemental operators are formed at every time step. This is necessary to handle the mesh shape variations in time. Since we do not have an effective preconditioner for the full implicit solver, we use the full direct Schur complement method for modal expansion order $N \leq 6$, and the iterative-boundary, direct-interior, Schur complement method for higher order modal expansions [7].

Bearing in mind the aforementioned caveats, we demonstrate the possible advantages of using the ALE formulation with the spectral element method—namely, the usual advantages of *low dispersion and high accuracy* and the novel fact that since the spectral elements are larger and less numerous than finite elements or finite volume cells, they can *support larger deformations without becoming entangled*. We will also show that the triangles can support deformation without losing excessive resolution.

2.1. *Formulation*

We consider the nondimensionalized incompressible Navier–Stokes equations with a passively advected scalar field. The domain is time-dependent ($\Omega(t)$), and it is moving with velocity $\mathbf{w}$. The governing equations are

$$\frac{\partial \mathbf{u}}{\partial t} + (\mathbf{u} - \mathbf{w}) \cdot \nabla \mathbf{u} = -\nabla p + \frac{1}{Re} \nabla^2 \mathbf{u} + \mathbf{f} \quad \text{in } \Omega(t) \tag{1}$$

$$\frac{\partial \theta}{\partial t} + (\mathbf{u} - \mathbf{w}) \cdot \nabla \theta = \frac{1}{Pe} \nabla^2 \theta \quad \text{in } \Omega(t) \tag{2}$$

$$\nabla \cdot \mathbf{u} = 0 \quad \text{in } \Omega(t), \tag{3}$$

where $\mathbf{u}$ is the fluid velocity, θ is the nondimensional temperature or normalized concentration density, $Re = \frac{U_o \rho h}{\nu}$ is the Reynolds number, Pe is the Peclet number, and $\mathbf{f}$ is a body force. The pressure is normalized ρU_o^2, where U_o, ρ, h, and ν are the reference velocity, fluid density, characteristic length, and kinematic viscosity, respectively. The Peclet number is the Reynolds number multiplied by either the Prandtl number (Pr: ratio of the momentum and thermal diffusivities) or the Schmidt number (Sc: ratio of the momentum and mass diffusivities), for heat transfer or species transport applications, respectively. For heat transfer problems, the nondimensional temperature is given as

$$\theta = \frac{T - T_o}{\Delta T},$$

where T_o is a reference temperature, and ΔT is a predefined or desired temperature difference. For the species transport applications, θ can be identified as the concentration density normalized by a reference value.

2.2. *Temporal Discretization*

The operator splitting scheme used in the new algorithm is an extension of a third-order stiffly stable time integration scheme developed by Karniadakis *et al.* [16]. Here, we present extensions of this formulation for the ALE algorithm, including the scalar transport equation. The splitting scheme involves these steps

$$\tilde{\mathbf{u}} = \sum_{q=0}^{Ji-1} \alpha_q \mathbf{u}^{n-q} + \Delta t \left(\sum_{q=0}^{J_e-1} \beta_q \mathbf{N}(\mathbf{u}^{n-q}, \mathbf{w}^{n-q}) + \mathbf{f}^{n+1} \right) \tag{4}$$

$$\tilde{\theta} = \sum_{q=0}^{Ji-1} \alpha_q \theta^{n-q} + \Delta t \left(\sum_{q=0}^{J_e-1} \beta_q \tilde{\mathbf{N}}(\mathbf{u}^{n-q}, \mathbf{w}^{n-q}, \theta^{n-q}) \right) \tag{5}$$

$$\mathbf{x}^{n+1} = \sum_{q=0}^{Ji-1} \alpha_q \mathbf{x}^{n-q} + \Delta t \left(\sum_{q=0}^{J_e-1} \beta_q \mathbf{w}^{n-q} \right) \tag{6}$$

$$\frac{\partial \bar{p}^{n+1}}{\partial n} = \mathbf{n} \cdot \left[- \sum_{q=0}^{J_e-1} \beta_q \mathbf{N}(\mathbf{u}^{n-q}, \mathbf{w}^{n-q}) - \frac{1}{Re} \sum_{q=0}^{J_e-1} \beta_q [\nabla \times (\nabla \times \mathbf{u}^{n-q})] \right] \tag{7}$$

$$\nabla^2 \bar{p}^{n+1} = \nabla \cdot \left(\frac{\tilde{\mathbf{u}}}{\Delta t} \right) \tag{8}$$

$$\nabla^2 \mathbf{u}^{n+1} - \frac{\gamma_0 Re}{\Delta t} \mathbf{u}^{n+1} = -\frac{Re}{\Delta t} (\tilde{\mathbf{u}} - \Delta t \nabla \bar{p}^{n+1}) \tag{9}$$

$$\nabla^2 \theta^{n+1} - \frac{\gamma_0 Pe}{\Delta t} \theta^{n+1} = -\frac{Pe}{\Delta t} \tilde{\theta} \tag{10}$$

$$\nabla^2 \mathbf{w}^{n+1} = 0, \tag{11}$$

where $\mathbf{x}(\mathbf{X}, t)$ are the coordinates of the moving frame, relative to a fixed set of coordinates $\mathbf{X}$ and

$$\mathbf{N}(\mathbf{u}, \mathbf{w}) = (\mathbf{u} - \mathbf{w}) \cdot \nabla \mathbf{u}, \tag{12}$$

$$\tilde{\mathbf{N}}(\mathbf{u}, \mathbf{w}, \theta) = (\mathbf{u} - \mathbf{w}) \cdot \nabla \theta. \tag{13}$$

The first four steps are explicit and computed using the values of θ, $\mathbf{u}$, $\mathbf{w}$, which are computed at the quadrature points using the methods outlined in [15]. The last four steps (Eqs. (7)–(11)) are computed in a variational framework. For example, the variational statement for the pressure equation is

Find $\bar{p} \in P^n$ that satisfies

$$(\nabla v, \nabla \bar{p}) = -\left(v, \nabla \cdot \left(\frac{\hat{\mathbf{u}}}{\Delta t} \right) \right) + \left(v, \frac{\partial \bar{p}}{\partial \mathbf{n}} \right)_{\Gamma_{\mathbf{u}}} \quad \forall v \in P^n \tag{14}$$

$$\bar{p} = 0 \quad \text{on} \quad \Gamma_{\mathbf{o}}, \tag{15}$$

where $\Gamma_{\mathbf{o}}$ is the set of outflow boundaries, and $\Gamma_{\mathbf{u}}$ is the set of boundaries with specified Dirichlet velocity boundary conditions. Details on the methods used to solve the matrix systems resulting from these kinds of elliptic variational statements can be found in [6].

The constants α_q, β_q in Eqs. (4)–(7) are integration weights and are defined in [16] (see also Table 6.1 in [6]). The mesh velocity is in general arbitrary and can be specified explicitly or can be obtained from a Laplace equation, following [14]. More recent work suggests a modified approach, where a variable coefficient is used in the Laplacian to provide enhanced smoothing, and thus, preventing sudden distortions in the mesh [13]. The incompressible Navier–Stokes and the scalar transport equations in an arbitrarily moving domain can be subject to various boundary conditions. To this end we considered various combinations of the Dirichlet and Neumann type conditions on stationary and moving surfaces. Applications of these boundary conditions to various transport problems are demonstrated in Section 4.

3. ALGORITHM VERIFICATION

The new algorithm is the thermal/ALE extension to the $\mathcal{N}\varepsilon\kappa\mathcal{T}\alpha\boldsymbol{r}$ family, originally developed by Karniadakis and Sherwin [6, 7]. The original $\mathcal{N}\varepsilon\kappa\mathcal{T}\alpha\boldsymbol{r}$ has been validated extensively by comparisons against the analytical solutions of the incompressible Navier–Stokes equations for stationary domains. In this section we present validation of the thermal/ALE version of the algorithm by demonstrating its time and space accuracy for moving/dilating domains. Since large mesh deformations in ALE algorithms may result in skew elements, it is important to demonstrate the convergence characteristics of the method for highly deformed elements. Therefore we first present a global convergence study for skew elements.

3.1. *Global Convergence in Skew Elements*

We now consider the effect of the skewness of the physical elements on the accuracy of the projection operator without any mesh motion. In Fig. 1, we examine eight different meshes consisting of triangles and quadrilaterals. We start by projecting $\sin(\pi x)\sin(\pi y)$ onto a square domain covered with standard elements. Figure 2 shows the results for the *modal* basis, demonstrating that exponential convergence is achieved. Subsequently, we make the elements covering the domain progressively more skewed in the B–H meshes. In each case, we see that exponential convergence is achieved, even when one of the triangular elements has a minimum angle of about 10^{-3} degrees (see Case H in Fig. 1). Hence, the accuracy of the method is extremely robust for badly shaped elements. Also, we note that the similarity of the convergence curves demonstrates that the rate of exponential convergence is unaffected by the skewing for meshes A–G.

3.2. *Convergence Studies of the Thermal/ALE Algorithm*

Here we verify the convergence characteristics of the current algorithm using Stokes' second problem: Fluid flow in a semiinfinite domain due to an oscillating plate. Our analysis also includes the wall temperature oscillations in phase with the wall velocity fluctuations.

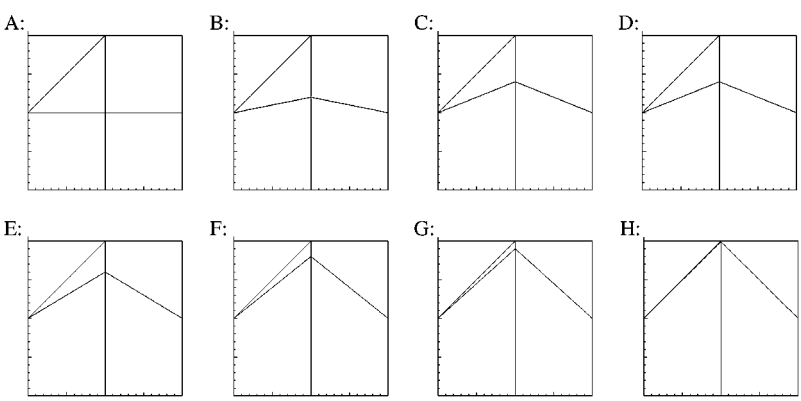

FIG. 1. Meshes (A–H) consist of three quadrilaterals and two triangles, which are progressively skewed by shifting the interior vertex. Case H results in element minimum angle of 10^{-3} degrees. Convergence plots for all these cases are shown in Fig. 2.

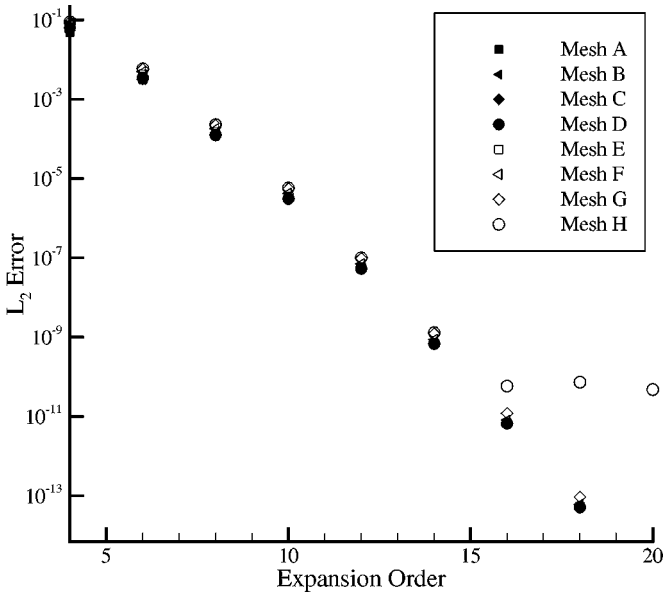

FIG. 2. Convergence in the L_2 norm for *modal projection* of the function $u = \sin(\pi x)\sin(\pi y)$ on meshes A–H shown in Fig. 1.

The boundary conditions on the wall ($y = 0$) are

$$u(y,t) = U_o \cos(\omega t),$$
$$\theta(y,t) = \theta_o \cos(\omega t),$$

where U_o and θ_o are the amplitudes of the nondimensional velocity and temperature, respectively. Both the temperature and velocity fluctuations have the oscillation frequency ω. Since the plate oscillates laterally, these boundary conditions can be imposed without an actual plate motion. The analytical solution for the temperature and velocity distributions are given as a function of time and space as

$$\begin{aligned} u(y,t) &= U_o \exp\left(-\sqrt{\frac{\omega}{2\nu}}y\right)\cos\left(\omega t - y\sqrt{\frac{\omega}{2\nu}}\right) \\ \theta(y,t) &= \theta_o \exp\left(-\sqrt{\frac{\omega}{2\alpha}}y\right)\cos\left(\omega t - y\sqrt{\frac{\omega}{2\alpha}}\right), \end{aligned} \tag{16}$$

where ν is the kinematic viscosity and α is the thermal diffusivity of the fluid.

We studied flow and heat transfer under three different conditions covering the stationary, laterally oscillating, and dilating domains shown in Fig. 3.

1. Stationary domain: Here the oscillations in wall velocity and temperature are handled via the time- and space-dependent boundary conditions without mesh motion. The mesh used in our calculations is shown in Fig. 3 (Case a). The side boundaries are periodic. In order to avoid moving the upper boundary very far away from the bottom surface, we imposed the analytical solution at the top surface.

2. Laterally oscillating domain: Here we allowed the computational domain to oscillate with the specified wall velocity and kept the top boundary stationary. Figure 3 (Case b)

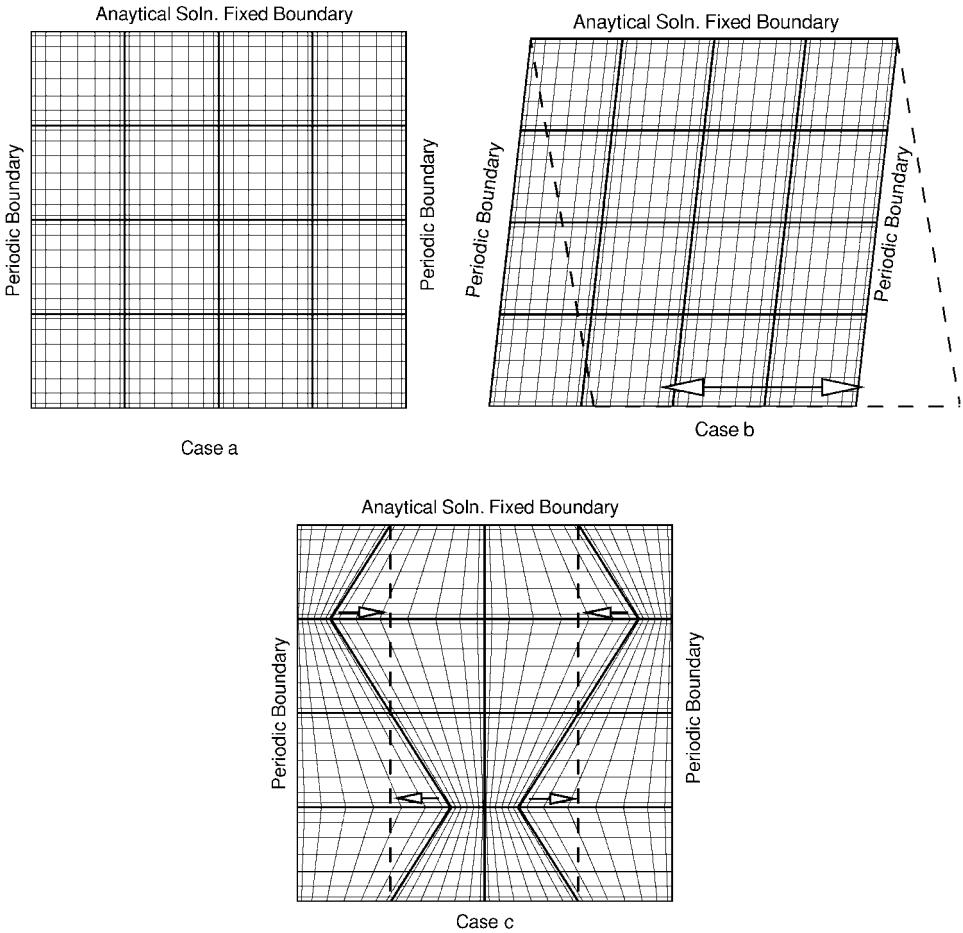

FIG. 3. Mesh utilized for code validation consisted of 16 spectral elements. The ALE algorithm is tested for stationary (Case a), laterally oscillating (Case b), and dilating domains (Case c). Snapshots of the maximum mesh deformation are shown for moving domains (Cases b and c). The elemental discretization is shown by the thick lines and quadrature points for eighth-order expansion are shown by the thin lines.

shows an instance where the mesh deformation is the maximum (the dashed lines show the mesh location half a period before the current position). The lateral deformation case does not impose any mesh dilation. However, it allows us to determine the behavior of the new algorithm during a "dilation-free" mesh motion.

3. Dilating domain: This is established by moving the four inner points of the mesh in a time periodic manner, while the top, bottom, and side boundaries are kept stationary. The wall boundary conditions are implemented without the plate motion. This is a general case. A snapshot of the computational grid at the maximum dilation position is shown in Fig. 3 (Case c). The maximum dilation is about 40% of the initial mesh configuration shown by the dashed lines. An ALE algorithm should honor the divergence-free velocity condition for incompressible flows, even under severe mesh dilation.

We tested the new ALE algorithm for the above three cases for various spectral expansion order N and time step Δt. We performed eight different simulations for each of the three cases. Both the time and spatial accuracy were established for the stationary, laterally

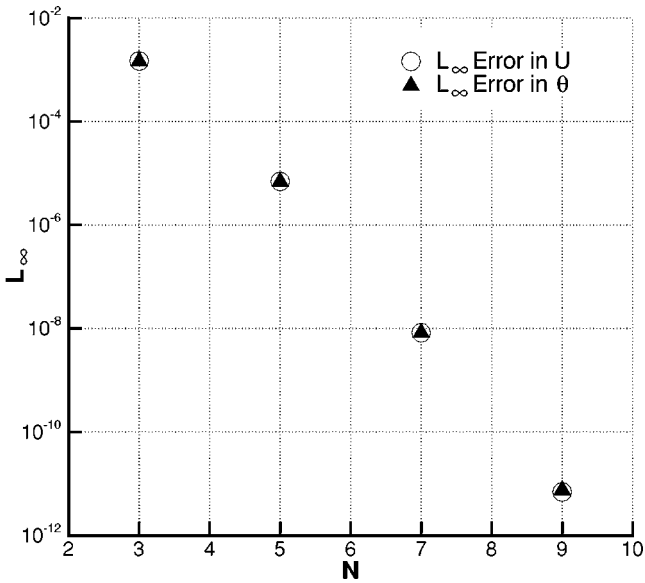

FIG. 4. Spectral convergence of the new ALE algorithm using a total of 16 elements with variable expansion order N. The problem is integrated until time $t = 1$, with time step $\Delta t = 10^{-5}$ using a third-order stiffly stable time integration scheme.

oscillating and dilating cases. For the space accuracy, we selected a very small time step ($\Delta t = 10^{-5}$) with third-order time accuracy and integrated our results until time $t = 1$, by varying the modal expansion order $3 \leq N \leq 9$. Figure 4 shows exponential decay of the L_∞ discretization error. This is spectral convergence, where doubling the degrees of freedom per direction results in *more than two orders of magnitude reduction* in the discretization errors.

We established time accuracy of the algorithm by keeping the modal expansion order $N = 7$, which guarantees the maximum spatial error to be 10^{-8}, and then systematically varying the time step Δt and running the code until time $t = 1$. The new algorithm allows up to third-order time accuracy. A sample time convergence plot is shown in Fig. 5. For this particular case, second-order time accuracy is demonstrated and is consistent with the integration scheme chosen in our numerical experiments. Only the results for the locally dilating domain (Case c) are shown in Figs. 4 and 5 for clarity. The results of the laterally oscillating and stationary mesh cases are similar to those shown in the figure, and they are not presented.

Stokes' second problem is not particularly challenging for studying the combined phase and dissipation error characteristics of the scheme, which may become important during long time integration of unsteady flows. Therefore we benchmark combined phase/dissipation error of a more challenging case next.

3.3. *Combined Phase and Dissipation Error Characteristics*

Reduction in phase and dissipation errors with increased spatial order of numerical schemes has been demonstrated earlier by Kreiss and Oliger [17]. This has been a justification for utilization of high-order methods, such as the spectral/*hp* methods used in this paper. In order to assess the combined phase and dissipation error of the algorithm, we examine error accumulation in long time integration of a convection diffusion equation.

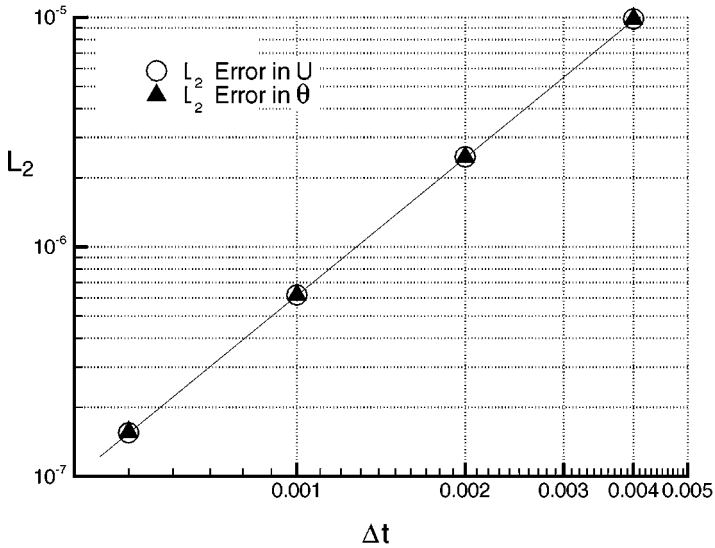

FIG. 5. Time convergence for the ALE algorithm. The results are integrated using a second-order, stiffly stable scheme until time $t = 1$. The spectral expansion order of $N = 7$ with 16 spectral elements is used. Second-order time accuracy is verified.

We establish this by solving the two-dimensional Navier–Stokes and scalar transport equations in a periodic box with moving internal mesh points for 10 time periods. The spectral element mesh and its motion are similar to Case c, shown in Fig. 3. However, the boundary conditions are periodic in all directions, unlike the case presented in the figure. The maximum mesh dilation is 40% of the initial configuration indicated by the dashed lines in Fig. 3, Case c. Since the mesh motion is not uniform in the spanwise direction, incorrect treatment of mesh motion and dilation may create two-dimensionality in the problem, even for one-dimensional convection diffusion equation. Hence, we choose the initial conditions of uniform velocity $\mathbf{V} = U_o \mathbf{e_x}$, and periodic streamwise temperature distribution $\theta(x)$. With these initial conditions and periodic boundary conditions in the spanwise and streamwise directions, two-dimensional Navier–Stokes and scalar transport equations are reduced to a one-dimensional convection diffusion equation given as

$$\frac{\partial \theta}{\partial t} + U_o \frac{\partial \theta}{\partial x} = \alpha \frac{\partial^2 \theta}{\partial x^2}. \tag{17}$$

The analytical solution for this equation can be obtained as

$$\theta(x, t) = \theta_o \sin(\omega(x - U_o t)) \exp(-\alpha \omega^2 t), \tag{18}$$

where $\theta_o = \sin(\omega x)$ is the initial condition and ω is the wave number. The domain length is unity. We specified the parameters $U_o = 1$, $\omega = 2\pi$. The diffusion coefficient is chosen $\alpha = 0.4/(2\pi)^2$ in order to reduce the diffusion effects; hence the wave can be maintained for a large number of time periods.

In Fig. 6, we present the evolution of phase errors in L_2 norm as a function of time. The time step is fixed at $\Delta t = 1.0 \times 10^{-4}$ and a third-order stiffly stable time integration scheme is utilized. There are 16 quadrilateral elements and the elemental modal expansion order N is successively increased from $N = 3$ up to $N = 9$. Considering the *exponential decay of the*

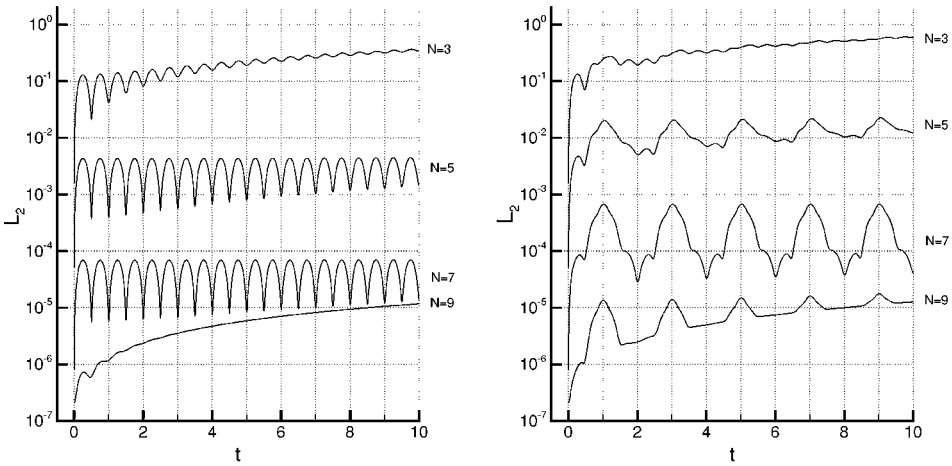

FIG. 6. Normalized L_2 phase/dissipation error variation with respect to time for various values of N. The left figure shows the error for a stationary domain, corresponding to Case a in Fig. 3. The right figure shows locally dilating mesh, which oscillates between the undeformed and deformed configurations of Case c in Fig. 3. The boundary conditions for this problem are periodic in the spanwise and streamwise directions.

analytical solution by time, the error also decreases exponentially. In order to circumvent this we normalize the error by dividing it with $\exp(-\alpha\omega^2 t)$ at any given time. Hence, the L_2 error norm shows the *normalized error* here. The results presented in Fig. 6 (left) correspond to the nondilating mesh. For $N = 3$ the spatial resolution is relatively poor and the error increases by time with a larger slope than that of the $N = 5$ and $N = 7$ cases. For $N = 9$, the time errors dominate over the discretization errors; hence we observe a different time history of error evolution until the 10th time period (we decreased the time step further and reran $N = 9$ case to verify this claim). Overall exponential decrease in the *normalized* error is observed for increased modal expansion orders (up to $N = 7$), indicating *spectral convergence* in the combined phase and dissipation error. It is noteworthy to indicate that the error evolution by time shows two spikes per time period. We believe this is due to the single wavelength chosen in the initial conditions.

The error evolution by time for the (locally) dilating grid is shown in Fig. 6 (right). The error for the locally dilating mesh is increased by an order of magnitude, compared to the stationary domain. Furthermore, the local characteristics of the L_2 error are dominated by the grid motion, which has a time period of 2. Effects of mesh motion are clearly seen in the right figure. Despite relatively larger errors, we still observe exponential decrease of the L_2 error at any given time with increased modal expansion order for $3 \leq N \leq 7$. For $N = 9$, time error dominates the convergence for $\Delta t = 1.0 \times 10^{-4}$, similar to the stationary grid case. These results demonstrate that *the rate of growth of phase and dissipation errors in time is reduced exponentially* with increased modal expansion order N, for both the static and the ALE spectral/*hp* algorithms.

4. APPLICATIONS

In this section, we present simulation results for coupled fluid flow and scalar transport (and heat transfer) in moving domains. The coupled interdisciplinary solution of mass, momentum, and energy transport is of great interest in many engineering and micro-fluidic

applications. Some applications of the new algorithm are demonstrated by species mixing simulations in a micro-mixer and time-periodic forced convection simulations in a micro heat spreader device.

4.1. *Micro-channel Mixing Promoted by an Oscillating Cylinder*

The main interest in micro-scale mixing devices is due to their potential use in biological and chemical sample preparation and pharmaceutical applications. Effective mixing due to turbulence cannot be observed in micro-scales, since most micro-flows correspond to low Reynolds number laminar or Stokes' flows. Hence, micro-mixers must utilize other mixing enhancement techniques. For example, mixing can be enhanced via chaotic advection obtained by pulsed source/sink systems, as demonstrated by Lee and Ho [18]. Their approach is effective for low Reynolds number laminar flows. Volpert *et al.* developed an alternative mixing strategy [19], which utilizes a set of cross-flow channels perturbing Stokes' flow in the main flow channel. Other micro-mixer designs based on peristaltic motion of viscous fluid confined in a rectangular cavity and bend-induced stirring have also been proposed [20, 21]. These approaches seem feasible for various applications.

In this work, we present the preliminary results for mixing of two fluids of same density in a micro-channel by stirring the fluid with an oscillating cylinder. Although detailed mixing studies require three-dimensional simulations, our preliminary results are intended to demonstrate the capability of the new algorithm, and they are limited to two-dimensional analysis. Two fluids are introduced at the channel entrance from separate inlets as shown in Fig. 7a. Fully developed flow conditions are assumed at the inlet, with parabolic velocity

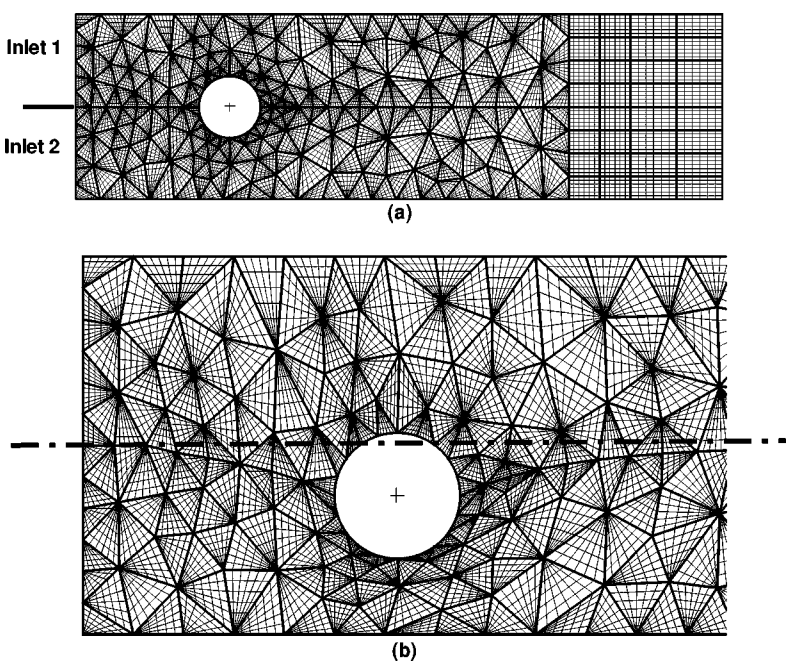

FIG. 7. The mesh used in mixing promotion utilized 32 quadrilateral and 314 triangular *hp* elements. The elemental discretization is shown by the thick lines and the quadrature points for sixth-order modal expansion are shown by the thin lines. The undeformed mesh is shown in (a). The deformed mesh at the cylinder minimum position, due to the cylinder oscillation, is shown in (b).

distribution and identical flow rates. The top stream carries a scalar quantity with concentration of $\theta = 1$, and the stream entering from the bottom has a concentration of $\theta = 0$. The zero-flux boundary conditions are used on the channel side walls and on the cylinder surface. The outflow boundary conditions specified at channel exit assumes partially fully developed conditions, where pressure is set to zero at the outflow, at one point.

The computational domain and the corresponding *hp* element discretization are shown in Fig. 7. We utilized a sixth-order modal expansion with 32 quadrilateral and 314 triangular *hp* elements. The total number of elements is fixed during a simulation. The elemental discretization is shown by the thick lines, and quadrature points are shown by the thin lines (Fig. 7a). Figure 7b shows the deformed mesh at the cylinder minimum position, caused by the cylinder oscillation. The dashed dotted line shows the center of the channel. The elements near the cylinder experience large deformations. Based on our previous test results (demonstrated in Figs. 1 and 2), it is clear that the unstructured *hp* mesh can sustain its high-order accuracy under such large deformations. Thus, we do not have to remesh the computational domain for most practical applications.

The oscillating cylinder perturbs the two streams with concentration densities of $\theta = 1$ and $\theta = 0$ and promotes mixing. Mixing of the two streams depends on the fluid's Schmidt number, $Sc = \nu/D$, where ν is the kinematic viscosity and D is the molecular diffusion coefficient. The ratio of fluid convection to mass diffusion is determined by the Peclet number (based on the mass diffusion coefficient). In this case the Peclet number in (2) is defined as $Pe = ReSc$. Since the mixing is promoted by the oscillating cylinder, the Strouhal number $St = U/\omega d$, defined by the maximum inlet velocity, the cylinder diameter d, and oscillation frequency ω, also becomes an important parameter in characterization of the micro-mixer. In this preliminary study, we fixed both the Reynolds ($Re = 100$) and Strouhal ($St = 0.6$) numbers and varied the Schmidt number. Two simulation results with $Sc = 1$ and $Sc = 5$ are shown in Figs. 8 and 9, respectively. A comparison of the two cases indicates sharper gradients in concentration densities for the increased Schmidt number. For the $Sc = 1$ case, the mass diffusion coefficient is relatively higher, and the concentration density contours are more diffused (see Fig. 8). We did not utilize any systematic measure of mixing in these preliminary studies.

Mixing simulations for large Schmidt number flows is more difficult than for the lower Schmidt number cases. The reason for this is the sharper concentration variations at the interface of the two fluids, making numerical solution increasingly more difficult to resolve. Low-order numerical methods exhibit increased numerical diffusion for underresolved simulations, to an extent that the numerical diffusion dominates over the physical diffusion, and the solution resembles a low Sc case. For high-order methods, such as the spectral/*hp* element method used in this work, underresolution of sharp gradients results in oscillations in the numerical solutions. Although this may seem to be a handicap of the spectral methods, oscillations in the solution can be used as indicators of the resolution quality of the mixing problem. In our preliminary simulations, the $Sc = 1$ case utilizes sixth-order modal expansion (Fig. 8). The concentration density contours for this case show no spurious oscillations, and thus, the simulations are quite well resolved. For the $Sc = 5$ case, we used eighth-order modal expansions. The contour plots for this case indicate *slightly* less-resolved spots at various locations. Lower expansion orders result in increased oscillations in the concentration density interface. On the other hand, the velocity and pressure fields, which depend on the Re and St, are well resolved for this case with $N = 5$. Our algorithm utilizes a single expansion order for the velocity and scalar fields, and the computational

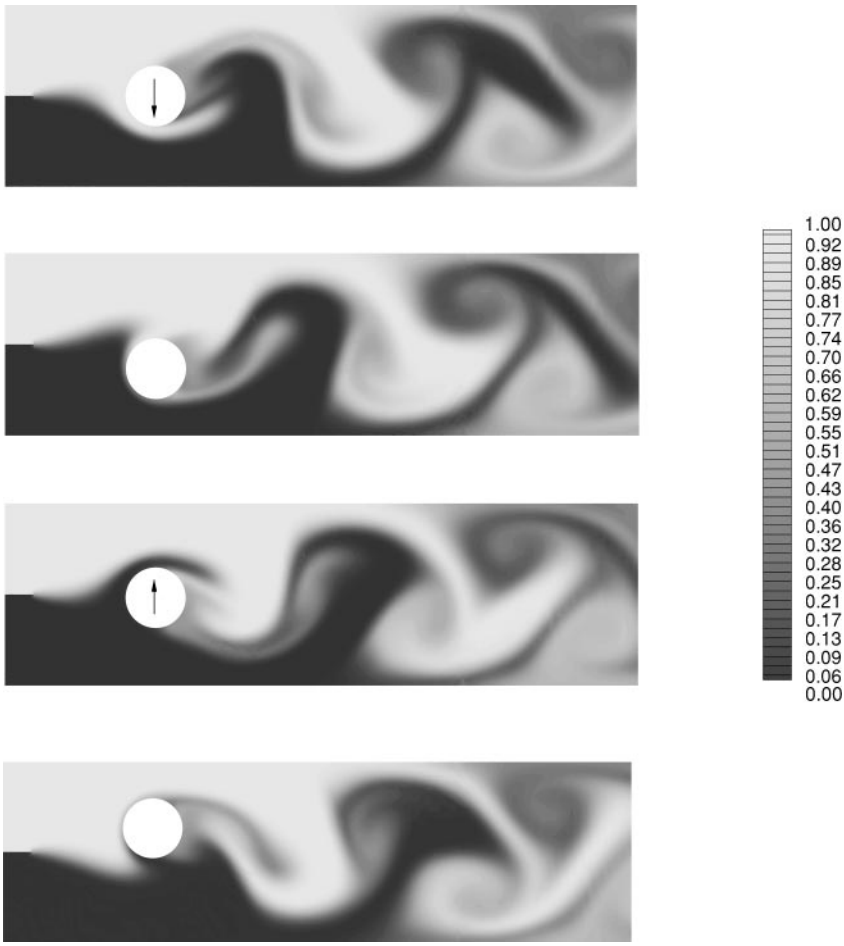

FIG. 8. Four snapshots for mixing promoted by an oscillating cylinder. The concentration density contours are shown for $Re = 100$, $Sc = 1$, $St = 0.6$. A total of 346 spectral/*hp* elements with sixth-order modal expansion are used in the simulations. Arrows show the direction of motion of the cylinder. The mesh configuration is shown in Fig. 7.

cost for solving the scalar transport field is about one fifth of the overall problem. Clearly a field-specific modal expansion procedure would be more efficient. For the $Sc = 5$ case, the computational efficiency would be increased by choosing $N = 5$ and $N = 8$ for the velocity and scalar fields, respectively. Implementation of two different modal expansion orders for the flow and scalar fields will increase the efficiency of the new module.

4.2. *Time-Periodic Forced Convection in Micro Heat Spreaders*

Efficient dissipation of concentrated thermal loads is a challenging problem in microelectronics applications. For example, inefficient heat dissipation from microelectronic components results in large chip surface temperatures, which commonly lead to chip malfunction. Thermal management problems of microelectronic components worsen with further miniaturization of the computers and increase in the central processing unit speeds.

We recently developed a new micro heat spreader concept [22], which consists of two reservoirs connected by a micro-channel, as shown in Fig. 10. Micro-membranes are

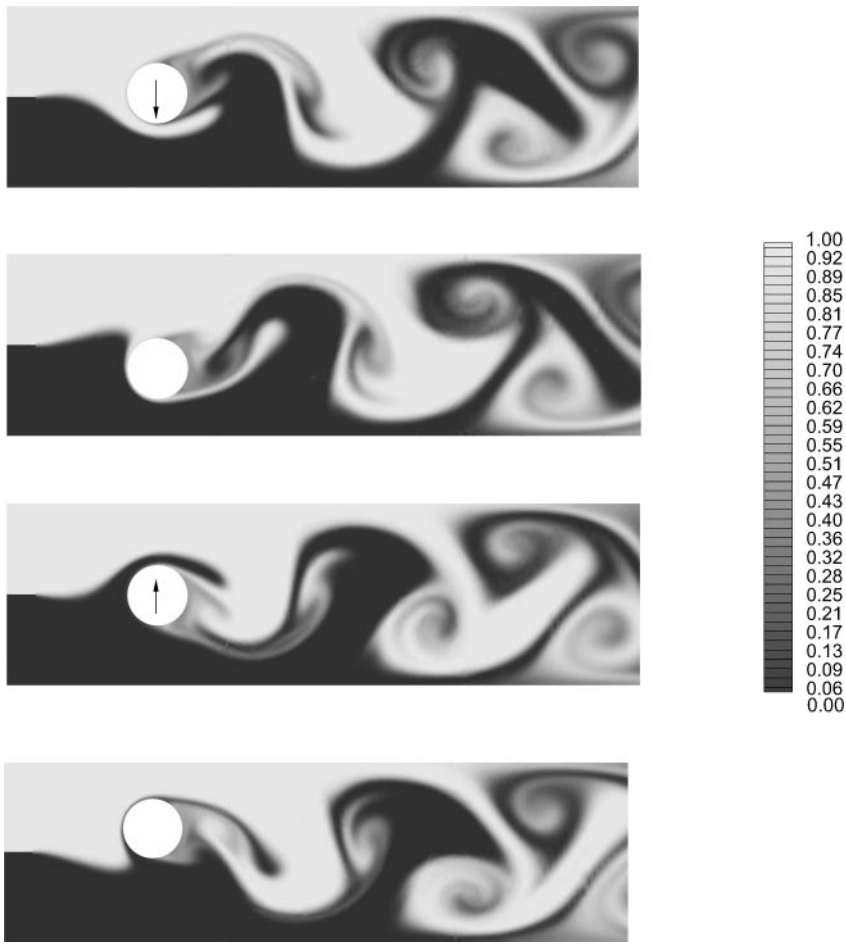

FIG. 9. Four snapshots for mixing promoted by an oscillating cylinder. The concentration density contours are shown for $Re = 100$, $Sc = 5$, $St = 0.6$. A total of 346 spectral/*hp* elements with eighth-order modal expansion are used in the simulations. Arrows show the direction of motion of the cylinder. The mesh configuration is shown in Fig. 7.

fabricated at the bottom sides of the reservoirs. Pumping action is generated by forcing the membranes with a phase difference of π either electrostatically or piezoelectrically. The micro-membranes pump the fluid from one reservoir to another in a continuous cycle. During the pumping cycle, heat generated by the source, located just above the micro-channel,

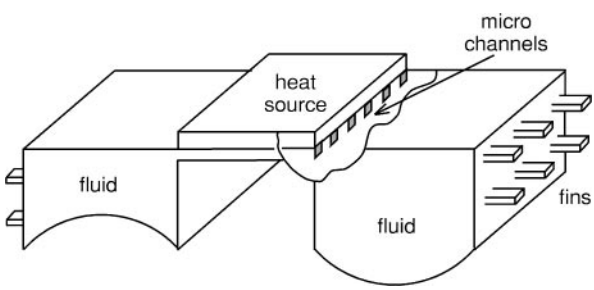

FIG. 10. Schematic view of the micro heat spreader device.

is conducted to the fluid. Because the height of the micro-channel is relatively small (on the order of 10 μm) the fluid heats very fast. As the hot fluid is pumped toward the exit of the micro-channel and into the receiving reservoir, the flow suddenly expands and starts to recirculate. This is desired to enhance mixing of the exiting hot fluid with the colder fluid in the mixing chamber. The pumping direction then reverses, and the procedure is repeated cyclically. This design allows two forced convection cooling passes per membrane cycle (left to right and right to left), with a resulting increase in the cooling efficiency. The fluid flow and heat transfer in this conceptual design is time-periodic.

We present two-dimensional preliminary simulations of fluid flow and heat transfer in the MHS device. The numerical simulations are performed as a function of nondimensionalized parameters such as the Reynolds, Prandtl, and the Strouhal numbers. Once the optimum parameters resulting in a minimum temperature variation of the MHS surface are determined, the actual device dimensions and the working fluid will be selected using the dynamic similarity. The preliminary results presented here are for $Pr = 10$ and $Pr = 1$, approximately corresponding to water and air, respectively. The Reynolds number is fixed at $Re = 2\pi$. The characteristic velocity within the closed system is based on the membrane oscillation amplitude and frequency, and thus, the Strouhal frequency of the simulations is unity. This choice of the characteristic velocity reduces the nondimensional parameters from 3 (Re, Pr, and St) to 2 (Re and Pr). The temperature contours at six different stages of its operation for $Pr = 10$ application are shown in Fig. 11. For this case, the MHS removes 68 W/cm^2 heat flux, with 10 K temperature difference between the heat source and the

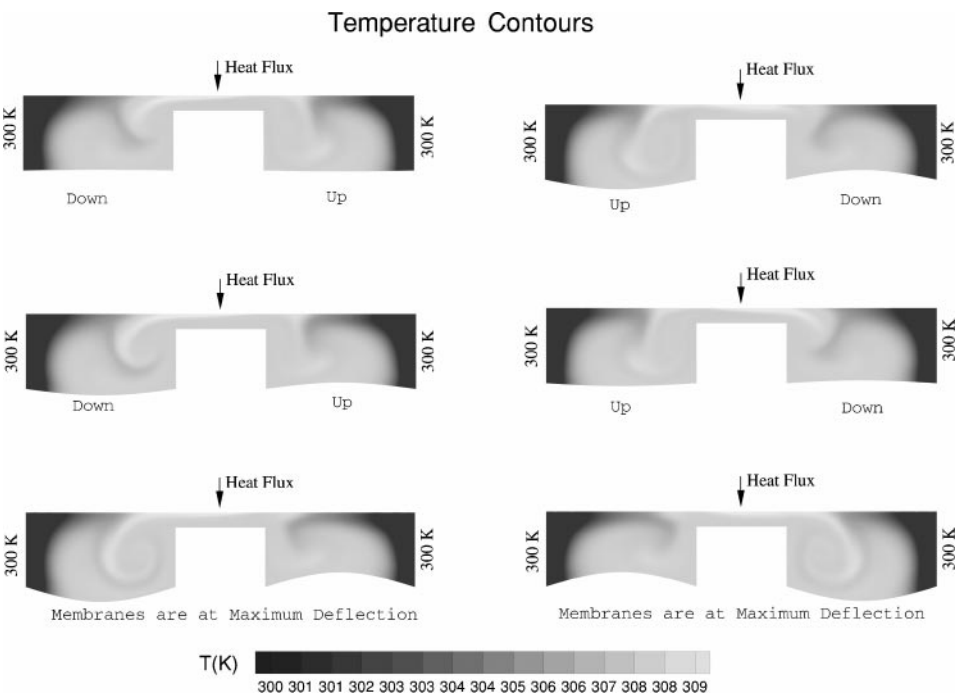

FIG. 11. Temperature contours for forced convection cooling via a micro heat spreader ($Re = 2\pi$, $Pr = 10$). The working fluid is water. Allowing 10 K temperature difference between the heat source and the side walls, 68 W/cm^2 heat flux can be removed. Direction of the membrane motion is shown vertically. Temperature contours at six equally spaced time intervals are shown.

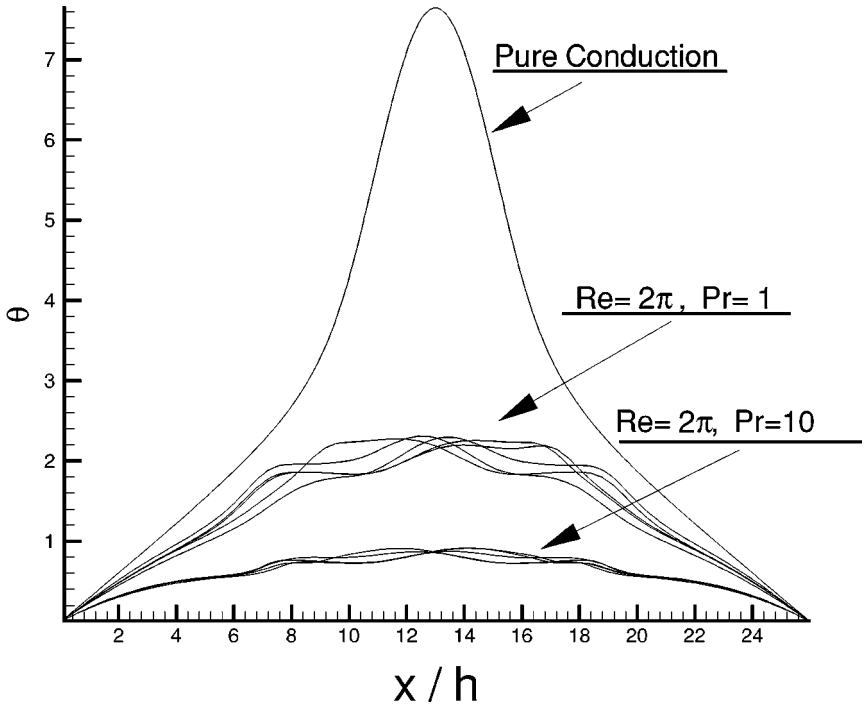

FIG. 12. Nondimensional temperature variation on the micro heat spreader top surface for five instances in time. The maximum nondimensional temperature for pure conduction cooling is about $\theta_{max} = 7.8$, for forced convection with $Re = 2\pi$ and $Pr = 1.0$, $\theta_{max} = 2.2$. For $Re = 2\pi$ and $Pr = 10.0$, $\theta_{max} = 1.0$ is obtained.

ambient. The MHS top surface temperature variations at five different instances are shown in Fig. 12. The maximum nondimensional temperature for pure conduction cooling is about $\theta_{max} = 7.8$; for forced convection with $Re = 2\pi$ and $Pr = 1.0$ the maximum temperature is reduced to $\theta_{max} = 2.2$. For $Re = 2\pi$ and $Pr = 10.0$, the maximum temperature is further reduced to $\theta_{max} = 1.0$. The results indicate considerable reduction in the maximum nondimensional surface temperature due to the time-periodic forced convection effects. Detailed analysis of the MHS devices is presented in [22].

5. SUMMARY AND CONCLUSIONS

We developed a spectral/*hp* element method based on the ALE formulation of two-dimensional Navier–Stokes and scalar transport equations in moving domains. The new algorithm uses a combined unstructured/structured grid, which offers great flexibility in mesh discretization. Spectral convergence characteristics of the algorithm allow utilization of relatively fewer degrees of freedom than low-order methods for a desired accuracy. This is an advantage in reduction and management of data. Also, utilization of relatively larger elements than the low-order methods enables spectral element ALE algorithms to sustain more severe mesh deformations than their low-order counterparts, reducing or eliminating the necessity for remeshing.

The thermal/fluidic transport problems have different diffusion/convection time scales. In the time-periodic examples of the MHS or micro-mixers, accumulation of phase and

dissipation errors can become problematic. Especially simulations for $Pr = 10$, compared to the $Pr = 1$ case, require approximately an order of magnitude increase in simulation time to reach time-periodic solutions. For long time-integration cases, spectral/hp methods exhibit exponential reduction in the time rate of growth of phase and dissipation errors. This constitutes an experimental justification for using high-order methods.

Finally, the new algorithm allows development of coupled interdisciplinary simulation tools for conceptual design and verification of micro electromechanical systems. The micromixer and the MHS examples given in this paper are purely conceptual devices, developed using the new ALE algorithm.

ACKNOWLEDGMENTS

We thank Professor George Karniadakis of Brown University for his support in development of the original hybrid $\mathcal{N}\varepsilon\kappa\mathcal{T}\alpha r$ code. We also thank Dr. Spencer Sherwin of Imperial College for supplying an early version of the original triangle-based $\mathcal{N}\varepsilon\kappa\mathcal{T}\alpha r$ and his valuable suggestions. A.B. acknowledges the partial financial support provided by Texas High Education Council, Advanced Research Projects Program Grant 000512-0418-1999, and T.C.W. thanks DARPA F49620-96-1-0426 and DOE DE-FG02-98ER25346 for their support.

REFERENCES

1. K. Gabriel, J. Jarvis, and W. Trimmer, *Small Machines, Large Opportunities.* Technical report (NSF Workshop on Micro Electromechanical Systems Research, 1987).
2. W. Trimmer, *Micromechanics and MEMS Classic and Seminal Papers to 1990* (IEEE Press, New York 1997).
3. A. Beskok, G. E. Karniadakis, and W. Trimmer, Rarefaction and compressibility effects in gas microflows, *J. Fluids Eng.* **118**, 448 (1996).
4. A. Beskok and G. E. Karniadakis, A model for flows in channels, pipes and ducts at micro and nano scales, *Microscale Thermophys. Eng.* **3**, 43 (1999).
5. P. Dutta, T. C. Warburton, and A. Beskok, Numerical modeling of electroosmotically driven micro flows, in *ASME Micro-Electro-Mechanical-Systems MEMS* (1999), Vol. 1, p. 467.
6. G. E. Karniadakis and S. J. Sherwin, *Spectral hp Element Methods for CFD* (Oxford Univ. Press, London, 1999).
7. S. J. Sherwin, *Triangular and Tetrahedral Spectral/hp Finite Element Methods for Fluid Dynamics*, Ph.D. thesis (Princeton University, 1995).
8. C. Canuto, M. Y. Hussaini, A. Quarteroni, and T. A. Zang, *Spectral Methods in Fluid Dynamics* (Springer-Verlag, Berlin/New York, 1988).
9. C. W. Hirt, A. A. Amsden, and H. K. Cook, An arbitrary Lagrangian-Eulerian computing method for all flow speeds, *J. Comput. Phys*. **14**, 27 (1974).
10. T. J. R. Hughes, W. K. Liu, and T. K. Zimmerman, Lagrangian-Eulerian finite element formulation for incompressible viscous flows, *Comput. Methods Appl. Mech. Eng*., 29:329, 1981.
11. J. Donea, S. Giuliani, and J. P. Halleux, An arbitrary Lagrangian-Eulerian finite element method for transient dynamic fluid-structure interactions. *Comput. Meth. Appl. Mech. Eng*. **33**, 689 (1982).
12. T. Nomura and T. J. R. Hughes, An arbitrary Lagrangian-Eulerian finite element method for interaction of fluid and a rigid body, *Comput. Meth. Appl. Mech. Eng*. **95**, 115 (1992).
13. R. Lohner and C. Yang, Improved ALE mesh velocities for moving bodies, *Comm. Num. Meth. Eng. Phys*. **12**, 599 (1996).
14. L.-W. Ho, *A Legendre Spectral Element Method for Simulation of Incompressible Unsteady Free-Surface Flows*, Ph.D. thesis (Massachusetts Institute of Technology, 1989).
15. T. C. E. Warburton, *Spectral/hp Methods on Polymorphic Multi Domains: Algorithms and Applications*, Ph.D. thesis (Brown University, Division of Applied Mathematics, 1999).

16. G. E. Karniadakis, M. Israeli, and S. A. Orszag, High-order splitting methods for the incompressible Navier–Stokes equations, *J. Comput. Phys.* **97**, 414 (1991).
17. H. Kreiss and J. Oliger, *Methods for the Approximate Solution of Time Dependent Problems*, GARP Publication Series (1973).
18. Y. K. Lee and C. M. Ho, Characterization of mixing process in a microchannel flow, in *Bulletin of the American Physical Society, Fluid Dynamics* (APS-DFD, 1999), Vol. 44, No. 8, p. 42.
19. M. Volpert, C. Meinhart, I. Mezic, and M. Dahleh, An actively controlled micromixer, in *MEMS Vol 1. Microelectromechanical Systems* (Am. Soc. Mech. Eng., New York, 1999), p. 483.
20. M. Yi, H. H. Bau, and H. Hu, A peristaltic meso-scale mixer. in *Micro-Electro-Mechanical Systems (MEMS) 2000* (Am. Soc. Mech. Eng., New York, 2000), p. 367.
21. M. Yi and H. H. Bau, The kinematics of bend-induced stirring in micro-conduits, in *Micro-Electro-Mechanical Systems (MEMS) 2000* (Am. Soc. Mech. Eng., New York, 2000), p. 489.
22. C. Sert and A. Beskok, Time-periodic forced convection in micro heat spreaders, in *Micro-Electro-Mechanical Systems (MEMS) 2000* (Am. Soc. Mech. Eng., New York, 2000), p. 375.